Journal of Materials Chemistry

Cite this: *J. Mater. Chem.*, 2012, **22**, 14180

www.rsc.org/materials

PAPER

Bottom-up assembly to Ag nanoparticles embedded Nb-doped TiO_2 nanobulks with improved n-type thermoelectric properties

Chengyan Liu,[ab] Lei Miao,*[a] Jianhua Zhou,[a] Rong Huang[c] and Sakae Tanemura[ade]

Received 9th March 2012, Accepted 21st May 2012
DOI: 10.1039/c2jm31469j

Nb-doped TiO_2-based nanostructures were novelly prepared by an economical and environmentally friendly hydrothermal method from TiO_2 and Nb_2O_5 powder precursors. The proposed formation mechanism is acceptable for the design of various Nb-doped TiO_2-based nanostructures. Furthermore, Nb-doped TiO_2 nanostructured bulk materials (nanobulks) embedded with Ag nanoinclusions were first fabricated by the bottom-up assembly of Ag_2O nanoparticles loaded Nb-doped TiO_2-based nanostructures. The introduction of Ag nanoparticles remarkably increased the Seebeck coefficient (S) of the TiO_2 bulk ceramic by 15% to 370 μV K^{-1} in the maximum case on account of the electron filtering effect. Moreover, their electrical conductivity (σ) was also improved by one order of magnitude up to 160 Ω^{-1} cm^{-1}, resulting from the contribution of both introducing Ag nanoparticles and Nb-doping. Finally, the figure of merit (ZT) was increased by about two-fold owing to the substantially optimized power factors ($S^2\sigma$). Our obtained results strongly confirm that the Ag embedded Nb-doped TiO_2 nanobulks can be used as good thermoelectric materials up to the high temperature of about 800 °C.

1. Introduction

Thermoelectric materials, which can convert heat directly into electricity efficiently and *vice versa*, become more and more fascinating as the energy crisis and environmental issues intensify. However, their applications are restricted mainly due to their high costs and low efficiencies. Furthermore, as common thermoelectric materials, Bi_2Te_3, PbTe, SiGe-based materials and complex "phonon glass electron crystal" (PGEC) materials[1] have all kinds of disadvantages though relatively high performance has been achieved. For example, some elements of the composition are rare in the Earth's crust, elementally harmful or instable under high temperature. Hence, transition metal oxide ceramics have attracted more and more attention owing to their good thermoelectric prospects, innocuity, low costs and excellent stability under high temperature.

Among the transition metal oxides that are promising thermoelectric materials, such as ZnO,[2] $SrTiO_3$,[3] TiO_2,[4] cobaltates,[5] *etc.*, TiO_2 might be considered as the prime candidate because it can be easily fabricated into various nanostructures with great potential thermoelectric applications.[6] Recently, there have been a few studies focusing on the thermoelectric properties of modified TiO_2 as in the following examples.[4,7,8] TiO_2 nanotubes covered with Te–Bi–Pb nanoparticles exhibit larger S than pure TiO_2 nanotubes.[7] Nb_2O_5 or Ta_2O_5 doped $(Ti_{0.75}Sn_{0.25})O_2$ ceramics show enhanced electrical conductivity and reduced lattice thermal conductivity (κ_l)[8] while the B-doping of rutile-type TiO_2 decreases both the electrical conductivity and thermal conductivity (κ).[4] Besides, modified TiO_2 is widely applied to photocatalysis,[9] solar cells,[10] gas sensors,[11] lithium ion batteries,[12] *etc.*

Usually, Nb-doped TiO_2 nanostructures have enhanced performance in applications.[13–16] However, in wet chemical preparations, which are more convenient in fabricating various nanostructures than physical methods, expensive and unstable niobium alkoxide or niobium chloride ($NbCl_5$) are always used as the precursors. Consequently, economical and easy processes should be investigated for the synthesis of Nb-doped TiO_2.

Up to now, the dramatic enhancements of ZT in nanobulks have come mostly from very large reduction of κ rather than the increase of $S^2\sigma$. So it is obvious that we will pay much more attention to the latter in seeking better performance materials. In 2008, Faleev and Léonard[17] proposed a theory to improve $S^2\sigma$, derived from the strongly energy-dependent scattering time of electrons at metal–semiconductor interfaces in metal–semiconductor nanobulks. Unfortunately, few materials that can be definitely improved by the introduction of metal nanoparticles have been reported so far.[18,19] To the best of our knowledge, metal–semiconductor nanobulks as essential n-type oxide

[a]*Key Laboratory of Renewable Energy and Gas Hydrate, Guangzhou Institute of Energy Conversion, Chinese Academy of Sciences, Guangzhou, 510640, P. R. China. E-mail: miaolei@ms.giec.ac.cn; Fax: +86-20-87035351; Tel: +86-20-87035351*
[b]*Graduate University of Chinese Academy of Sciences, Beijing, 100049, P. R. China*
[c]*Key Laboratory of Polarized Materials and Devices, Ministry of Education, East China Normal University, Shanghai 200062, P. R. China*
[d]*Japan Fine Ceramics Center, 2-4-1 Mutsuno, Atsuta-ku, Nagoya, 456-8587, Japan*
[e]*Powder Technology PJ Laboratory, Nagoya Institute of Technology, Gokiso-cho, Showa-ku, Nagoya, 466-8555, Japan*

thermoelectric materials for integrated thermoelectric devices have not been reported. In addition, cermet composites usually boost fracture toughness,[20] which is beneficial to the machining of brittle ceramics. Undoubtedly, these types of nanobulks with potential for thermoelectric applications are attractive.

For this study, we first used economical and stable TiO_2 and Nb_2O_5 powders as the precursors to synthesize Nb-doped TiO_2-based nanostructures *via* hydrothermal reactions. The products of this process are mixtures of Nb-doped titanate nanotubes and nanosheets, and they can be easily transformed into Nb-doped TiO_2 nanoparticles by a heat treatment procedure in air, which is obviously favoured over the frequently used expensive and environmentally harmful methods. Then, by applying a brilliant bottom-up assembly,[21] Ag_2O nanoparticle loaded Nb-doped titanate nanostructures were successfully fabricated into nanobulks. The obtained thermoelectric properties confirm that the proposed nanobulks have large potential for use in a relatively high temperature range up to about 800 °C.

2. Experimental section

2.1. Materials

Commercial titanium dioxide (TiO_2, 7 nm) with anatase phase (ST-01, Ishihara) and niobium(v) oxide (Nb_2O_5) with 99.99% metal basis (Aldrich) were used without further purification. Diluted sodium hydroxide (NaOH), hydrochloric acid (HCl) and silver nitrate ($AgNO_3$) solutions were prepared by mixing their corresponding analytical reagents (Guangzhou Brand) with deionized water.

2.2. Synthesis of Nb-doped TiO_2-based nanostructures

An alkaline hydrothermal method similar to our previous works[22,23] was applied to synthesize non-doped and Nb-doped TiO_2-based nanostructures. At first, 1.92 g of TiO_2 and various quantities of Nb_2O_5, the atomic ratio of Nb to (Nb + Ti) for the starting materials is presented by the variable x, were poured into 10 M NaOH aqueous solutions (160 ml), which were stirred vigorously by a magnetic bar. Ten minutes later, the mixture was transferred into a 400 ml Teflon-lined autoclave aided with a magnetic mixer (40 RPM) and kept at 150 °C for 40 h. After hydrothermal reaction, the white precipitates were collected and washed with deionized water until the pH values reached about 9. In order to prepare protonated non-doped and Nb-doped TiO_2-based nanostructures, a part of products were further immersed in 0.1 M HCl solutions (400 ml) with vigorous stirring at room temperature for 2 h, and then rinsed again by deionized water until neutral. Finally, all products were dried in air at 120 °C for 2 h.

2.3. Preparation of Ag_2O nanoparticle loaded titanate nanostructures

The obtained powders without the acidic bath (pH ≈ 9) were soaked in various $AgNO_3$ solutions, the concentrations of the $AgNO_3$ solutions are represented by the variable y, at 60 °C for 46 h (pH < 5). Then, the faint yellow sediments were washed by 600 ml deionized water followed by being dried at 120 °C in air for 2 h.

2.4. Compaction of powders to nanobulks

To study the thermoelectric properties, the desiccative Ag^+ ion exchanged nanostructures and protonated non-doped titanate nanotubes were pressed into rectangular bars and disks by cold-pressing procedures with a pressure of 1.5×10^5 kgf cm^{-1}. All bulk materials were sintered in a pure N_2 atmosphere at a constant heating rate of 5 °C min^{-1} to 1100 °C and kept under this condition for 10 hours in a tube furnace, where the samples were put on a graphite boat. After cooling naturally to room temperature, the Ag sediments on the surface of bulk materials were removed by a grinding blade and the samples were polished and incised for the thermoelectric characterizations. The nanobulks are denoted Ag_y–$Ti_{1-x}Nb_xO_2$ in this paper.

2.5. Characterization techniques

XRD patterns were collected on a powder diffractometer (PANalytical X'pert Pro MPD operated at 40 KV and 40 mA, Cu Kα radiation, $\lambda = 0.154$ nm) with a scanning step of 0.008° (2θ). FTIR transmission spectra were recorded on a Bruker TENSOR 27 spectrometer after the mixture of prepared powders and KBr granules had been pressed into wafers. Raman scattering spectra were studied on a JASCO NRS 2100 at room temperature and a 488 nm laser line was used as the excitation source. N_2 adsorption–desorption experiments were carried out at 77 K (Quantachrome, autosorb-1) after the samples had been outgassed at 250 °C for 6 hours. SEM and EDX characterizations were performed on a Hitachi S-4800 FESEM instrument equipped with an Oxford energy dispersive X-ray detector. TEM observations were executed on a JEOL-2100 microscope at 200 kV. Electrical resistivity and Seebeck coefficient were measured by the static DC method (ULVAC-RIKO, ZEM-3) under low argon (99.999%) atmosphere with temperature gradients of 20 °C, 30 °C and 40 °C. The thermal conductivity was calculated by using the formula: $\kappa = \alpha\omega c_p$, where α, ω and c_p represent thermal diffusivity, density and specific heat capacity, respectively. The heat capacity was measured by a differential scanning calorimetry (TA Instruments, DSC-2910), thermal diffusivity was investigated by a laser-flash method (ULVAC-RIKO, TC-9000V) and density was estimated by the Archimedes' methods. Carrier concentration (n_e) was surveyed by Hall-effect measurements with a van der Pauw electrode configuration under a vacuum of 10^{-3} Pa (Toyo Technica, Resi Test-8300).

3. Results and discussion

3.1. Products of the hydrothermal reactions and formation mechanism

The XRD patterns of nanostructures (pH ≈ 9) after alkaline hydrothermal treatments are displayed in Fig. 1a. It is observed that the non-doped sample has the typical diffraction peaks observed in sodium titanate nanotubes.[23–25] However, all peaks are weakened by the addition of Nb_2O_5, especially the characteristic reflection at about 10°, which corresponds to the spacing between neighboring TiO_6 octahedron layers of the nanotube walls.[24] Meanwhile, no other materials are detected until the quantity of incorporated Nb_2O_5 reaches about $x = 0.30$, where

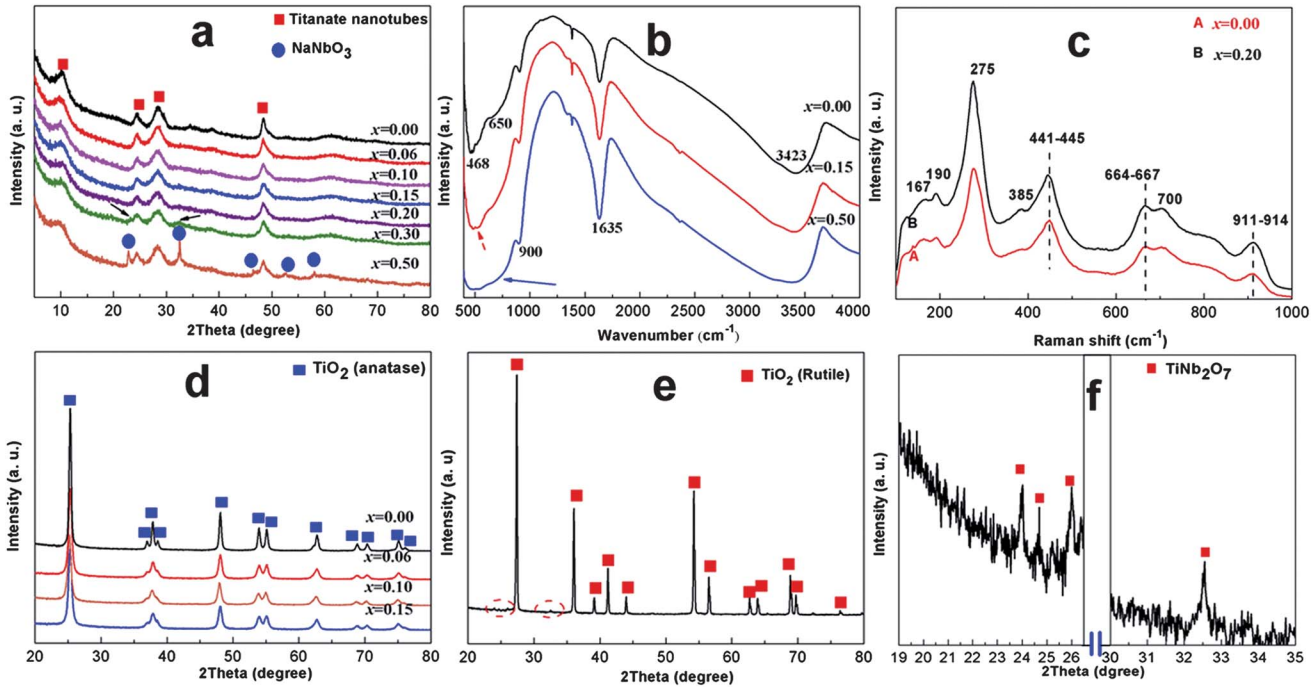

Fig. 1 (a) XRD, (b) FTIR transmission spectra and (c) Raman scattering spectra of the non-doped and various Nb-doped nanostructures (pH ≈ 9). (d) XRD of parts of the protonated samples after heat treatments at 600 °C in air for 4 h. (e) XRD of the protonated sample with $x = 0.15$ after heat treatment at 900 °C in air for 4 h. (f) Enlarged XRD of the regions marked by dot ellipses in (e).

some peaks of $NaNbO_3$, as indicated by the black arrows in Fig. 1a, appear. Therefore, Nb atoms might be intercalated into the space between TiO_2 octahedron sheets. The introduction of additive disturbed the crystallization process during the hydrothermal reactions.

According to FT-IR spectra shown in Fig. 1b, the absorption at around 3423 cm^{-1} can be attributed to the stretching vibrations of hydroxyl groups, and the absorption at 1635 cm^{-1} is associated with the H–O–H deformation vibration of the physisorbed water.[26] These phenomena demonstrate that a large amount of adsorbed water and a large number of hydroxyl groups exist in the products. As in earlier reports,[26,27] the absorption bands near 900 cm^{-1} and 650 cm^{-1} are observed for all samples without acid treatment due to the existence of Na^+ ions. At lower wave numbers, the peak near 468 cm^{-1} has been assigned to the Ti–O–Ti vibrations of the interconnected octahedra.[27] The band near 468 cm^{-1} indicated by the dotted arrow in Fig. 1b broaden with increasing Nb content. This may be attributed to the existence of Nb–O bonds.[28] In particular, a absorption region characteristic of $MNbO_3$ (M = Li, Na and K) at about 500–800 cm^{-1} appears in the sample of $x = 0.50$ as marked by the solid arrow in Fig. 1b, and thus agrees with the result of the XRD study.[29]

The Raman spectra show broad bands near 167, 190, 275, 385, 441, 664, 700 and 914 cm^{-1} as given in Fig. 1c. These agree well with the previous literature on titanates.[30] No distinct peaks of sodium niobate[31] and niobium pentoxide[32] can be found even at values of x up to 0.20, which have been revealed by the XRD patterns of Fig. 1a. There are slight shifts indicated by vertical dotted lines for the bands at around 441, 664 and 911 cm^{-1} between the two represented samples. These bands have been assigned to the internal vibrations of the TiO_6 octahedra, the Ti–O vibrations of anatase and the symmetric stretching mode of a short Ti–O bond in sodium titanate, respectively.[30] It seems that these changes are also induced by the Nb–O bonds. On the basis of these observations, it is most likely that Nb atoms are bonded with O atoms, but they are amorphous.

It may be more convenient to infer their structures from the characterization after heat treatment in air because of the better response of XRD to improved crystallinity. Based on this, thermal treatment under various temperatures in air were applied to the protonated samples. The XRD patterns of the heated samples are shown in Fig. 1d and e. Clearly, all protonated nanostructures ($x < 0.20$) are converted to the anatase phase without any impurities (see Fig. 1d) after heat treatment at 600 °C for 4 h. The crystallite size of the samples ($x < 0.20$) was estimated as listed in Table 1 by using the Debye–Scherrer equation. The crystallite size is suppressed significantly for the Nb-doped samples. In addition, the diffraction peaks slightly shift to lower degrees for these samples. It is also worth noting that weak reflections indexed to $TiNb_2O_7$ (see Fig. 1f) are

Table 1 Crystallite sizes estimated by Debye–Scherrer equation based on the peak of (101) of the sample shown in Fig. 1d

Samples	Crystallite size (nm)
$x = 0.00$	27.4
$x = 0.06$	15.9
$x = 0.10$	15.1
$x = 0.15$	14.9

obtained for the sample with $x = 0.15$ which has been transformed from anatase into the rutile phase (see Fig. 1e) at 900 °C. These results fit well with the conclusion of D. Wu *et al.*[33] which focuses on Nb-doped TiO_2 powders, and we can be assured of the successful substitution of Ti to Nb.

Accordingly, it might be concluded that Nb atoms are dispersed in titanate nanostructures in disorganized states but bonded to adjacent O atoms.

The shapes and morphologies of the nanostructures were characterized by using FESEM as given in Fig. 2, N_2 adsorption–desorption analysis as in Fig. 3 and TEM as in Fig. 4. From Fig. 2a and 4a, the non-doped sodium titanate nanostructures are mainly nanotubes with large aspect ratio. However, mixtures of nanotubes and nanosheets are obtained for the Nb-doped samples (see Fig. 4b). This relatively poor yield of nanotubes is attributed to the fact that the process of nanosheets scrolling into nanotubes during hydrothermal synthesis is hindered by the additive. In particular, these mixtures are glued together to form small agglomerations, and furthermore this phenomenon seems to be more and more highlighted with the increasing of atomic ratio (x) as observed in Fig. 2b and c. These SEM images suggest that the exfoliation of layered nanosheets is not perfect so that they are connected with each other locally. There are some peculiar nanoparticles with diameters of about 10–30 nm accumulating on the surface of the nanostructure for the specimen with $x = 0.20$ in the case of Fig. 2d. These particles are amorphous in the TEM image as displayed in the inset of Fig. 2d. It may indicate that the excess addition of Nb_2O_5 results in the crystallization of $NaNbO_3$ from amorphous particles for the continuous increasing of x, and this corresponds to the result of the XRD study for the sample with $x = 0.30$.

N_2 adsorption–desorption tests provide us with the auxiliary evidence to support the discussion as described above. Fig. 3a and b show N_2 adsorption–desorption isotherms and the corresponding pore size distribution curves of non-doped and Nb-doped nanostructures. The hysteresis loops shift to the region of higher relative pressure and their areas decrease as the Nb content increase, suggesting that the BET surface areas and pore volumes decrease as listed in Table 2 owing to the generation of lots of nanosheets during the hydrothermal reactions. All the samples have single pore size distributions with the maximum at about 3.8 nm, which might correspond to the size of pores inside the nanotubes. Consequently, we reconfirm the existence of nanotubes.

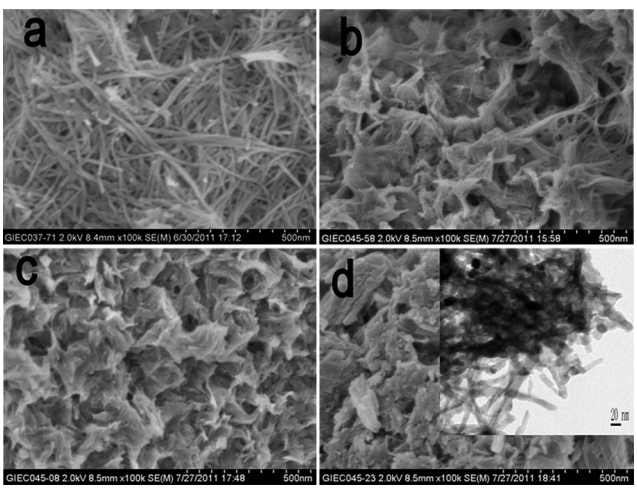

Fig. 2 SEM images of the samples (pH ≈ 9) with different Nb content: (a) $x = 0.00$, (b) $x = 0.06$, (c) $x = 0.15$, (d) $x = 0.20$ after hydrothermal reactions at 150 °C. Inset in (d) shows the corresponding TEM image with 20 nm scale bar of amorphous particles.

The HRTEM images shown in Fig. $4b_1$–b_3 and the inset of Fig. 4a could provide more detailed information for the damage effect of Nb_2O_5 to the formation of nanotubes. There are two disparate areas in both nanotubes and nanosheets in the Nb-doped sample, namely, well ordered (see the areas of 1 in Fig. $4b_1$ and b_2) and poorly ordered (see the areas of 2 in Fig. $4b_1$ and b_2) regions. On the contrary, the non-doped nanotubes seem to be better organized as shown in the inset of Fig. 4a. This may be explained as follows. Under the hydrothermal conditions of our experiments, Nb_2O_5 tends to form perovskite $NaNbO_3$,[34] which has a corner-sharing NbO_6 octahedron block. On the other hand, it is believed that TiO_2 is transformed into monoclinic titanate,[35] orthorhombic titanate[36] or anatase[37] during hydrothermal treatments, in all of which edge-sharing TiO_6 octahedra are essential. This difference might result in poor crystallization for the simultaneous precipitation of Ti^{4+} and Nb^{5+}. It is remarkable that the trumpet-like nanostructure composed of nanosheets, nanotubes and nanowires is observed as shown in Fig. $4b_3$. This unique morphology is the first such found for titanate nanostructures. We propose that short nanotubes were generated during the hydrothermal reactions,[24] and then these nanotubes became longer and longer by growing at both ends. However, for this trumpet-like nanostructure, the diameter of the short nanotube at one end is larger than that at the other end as displayed in the area of 2 in Fig. $4b_3$, which could be ascribed to the interference of the additive or other fluctuation factors. Therefore, the end with small diameter is likely to become closed while the other would epitaxially grow into curly nanosheets because a larger inner diameter is unstable for the nanotube.

Reviewing the present results and adopting some conclusions from earlier studies,[32,34,38] the possible formation mechanism of Nb-doped nanostructures in the hydrothermal processes can be proposed. The schematic of it is illustrated in Fig. 5. The outmost part of the TiO_2 powders is dissolved at first and then recrystallized into lamellar sodium titanate because TiO_2 powders can be synthesized into nanosheets at low hydrothermal temperatures (<60 °C)[24,38] while Nb_2O_5 powders are still inert even at 100 °C.[32,34] As the lamellar sodium titanate grows to be large enough, thin multiwall nanosheets tend to peel off. These fragments are flexible enough to scroll into short nanotubes, the driving force arising from mechanic tension[39] and/or the fluctuation of surrounding conditions.[37a] However, once the hydrothermal temperature rises to the critical point thus activating Nb_2O_5, the residual TiO_2 and Nb_2O_5 dissolve and precipitate simultaneously. The new generated lamellar sodium titanate contains both TiO_6 and NbO_6 octahedra. The different structures of their stable forms result in poor crystallized regions where O–M–O (M = Nb or Ti) bonds break the parallel layers or enhance local coalescence. This local coalescence is more rigid than the electrostatic attraction, which is induced by sodium ions between layers in sodium titanate, so the scrolling of nanosheets into short nanotubes is hindered. At last, the agglomerated

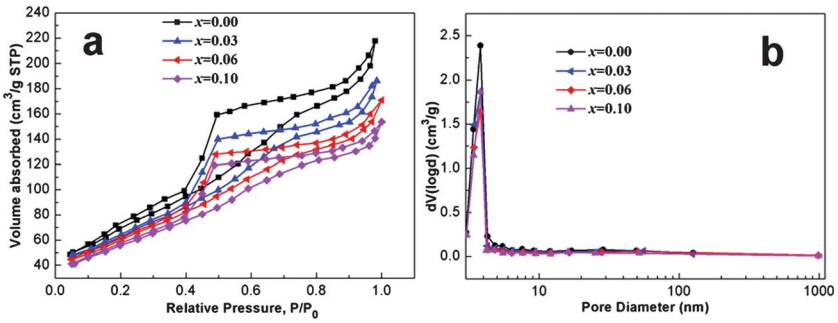

Fig. 3 (a) N_2 adsorption–desorption isotherms and (b) corresponding pore size distributions of non-doped and Nb-doped nanostructures (pH ≈ 9). The pore size distributions were determined by using the Barret–Joyner–Halender (BJH) method on desorption branches.

Nb-doped nanosheets with large aspect ratio are obtained after the hydrothermal treatments. On the other hand, the short titanate nanotubes formed at the very beginning might retain their nanotubular structure during the subsequent Nb-doping growth process even though their crystallinity suffers from the disturbance. It is worth pointing out that the concentration of dissolved Nb^{5+} ions in alkaline solutions during the hydrothermal reactions might not be uniform in the autoclave and may be time-dependent, which could be responsible for the formation of designated inhomogeneous poor ordered regions. This proposed formation mechanism may provide a guide to tailor various Nb-doped TiO_2-based nanostructures.

3.2. Ag_2O nanoparticle loaded titanate nanostructures

Now, we mainly focus on the ability of hydrothermal products to load Ag_2O nanoparticles with small sizes, which is favorable to the fabrication of Ag nanoparticle embedded nanobulks.

Table 2 BET surface areas and total pore volumes of non-doped and Nb-doped nanostructures (pH ≈ 9)

Samples	BET surface area ($m^2\ g^{-1}$)	Total pore volume ($cm^3\ g^{-1}$)
$x = 0.00$	261.014	0.365
$x = 0.03$	238.593	0.250
$x = 0.06$	225.498	0.215
$x = 0.10$	203.534	0.214

The impregnative aqueous ion exchange method is widely applied to prepare Ag nanoparticles loaded titanate nanostructures.[40,41] It is believed that the process contains three steps:[41] (1) Ag^+ ions are exchanged with Na^+ or H^+ ions on the outer and inner surfaces, (2) absorbed Ag^+ ions are deposited on the surface of the titanate nanostructures in the form of Ag_2O, and (3) the Ag_2O is thermally, chemically or photochemically reduced to Ag nanoparticles.

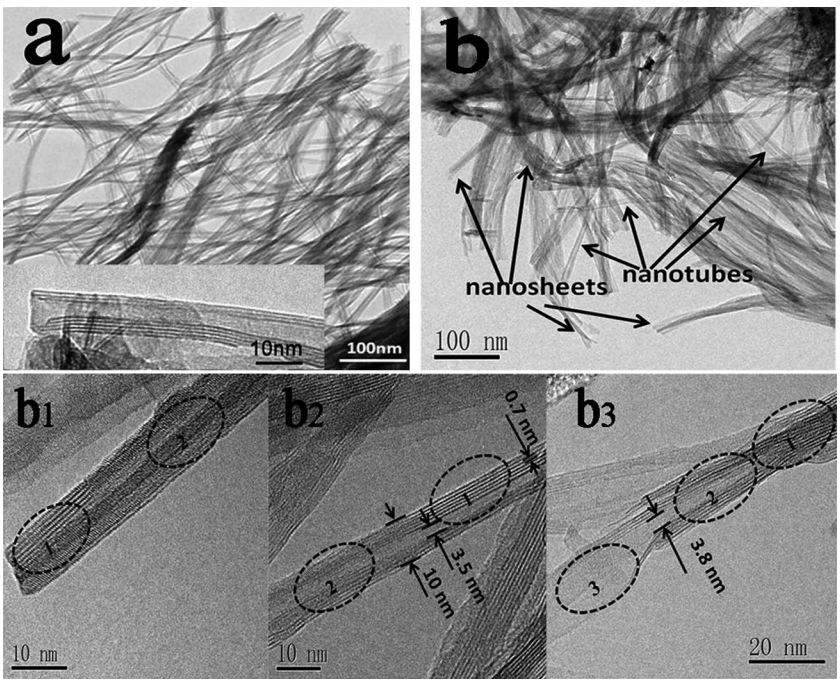

Fig. 4 TEM micrographs of the samples (pH ≈ 9) with different Nb content: (a) $x = 0.00$ and (b) $x = 0.06$. Inset in (a) shows its corresponding HRTEM image (a single nanotube). High-magnification images of a (b_1) nanosheet, (b_2) nanotube and (b_3) peculiar trumpet-like nanostructure composed of nanosheets, nanotubes and nanowires for the sample with $x = 0.06$.

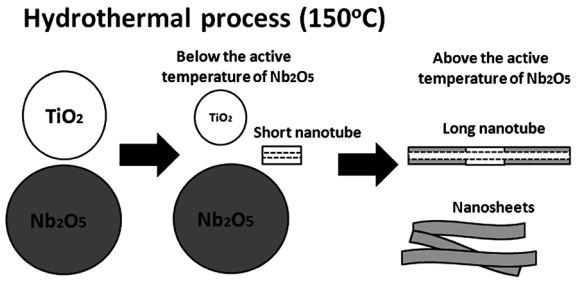

Fig. 5 Schematic illustration of the possible formation mechanism for a Nb-doped titanate nanotube and Nb-doped titanate nanosheets. Before the hydrothermal temperature reached the active point of Nb_2O_5, some short pure sodium titanate nanotubes had been generated. However, the formation of short nanotubes was interrupted when the temperature was high enough to activate Nb_2O_5.

Fig. 6b and c illustrate the SEM morphologies of the non-doped Ag^+ ion exchanged sample with $x = 0.00/y = 0.05$ and $x = 0.00/y = 0.20$, respectively. Apparently, these Ag^+ ion exchanged samples appear as more compact materials compared with the protonated sample with $x = 0.00/y = 0.00$ (see Fig. 6a) whose fibrous shape is nearly the same as the parent sodium titanate nanotubes as shown in Fig. 2a. Moreover, the degree of compaction seems intensified as a function of the increased concentration of the $AgNO_3$ solutions when the other conditions are unchanged. The Nb-doped sample with $x = 0.06/y = 0.05$ as shown in Fig. 6d also has a more compact morphology in contrast to its precursor (see Fig. 2b). These results may be associated with the precipitated nanoparticles on the surface of the titanate-based supports as displayed in Fig. 6e and f for the sample with $x = 0.00/y = 0.05$ and $x = 0.06/y = 0.05$, respectively. It can be recognized that small nanoparticles with a maximal diameter of about 10 nm decorate the bundles of both non-doped titanate nanotubes and Nb-doped titanate nanostructures.[41]

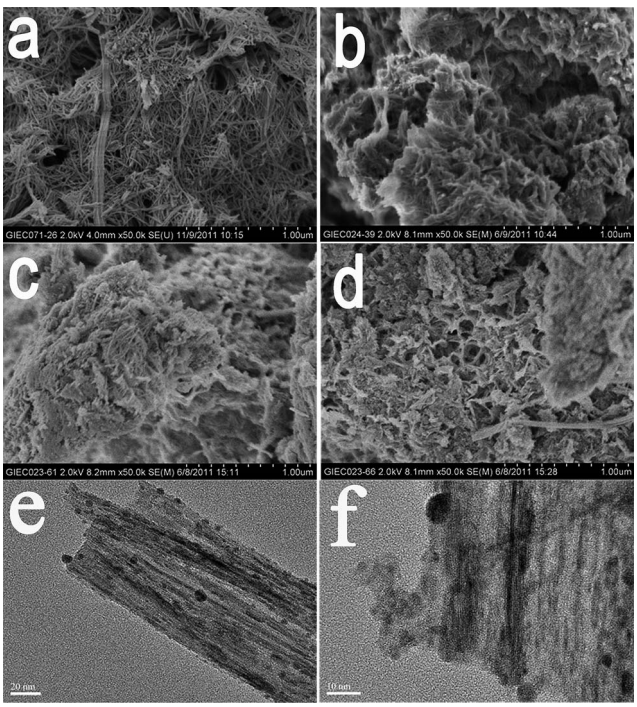

Fig. 6 SEM images of the (a) protonated sample with $x = 0.00/y = 0.00$ and Ag^+ ions exchanged sample with (b) $x = 0.00/y = 0.05$, (c) $x = 0.00/y = 0.20$ and (d) $x = 0.06/y = 0.05$. TEM images of the Ag_2O nanoparticle loaded samples with (e) $x = 0.00/y = 0.05$ and (f) $x = 0.06/y = 0.05$.

Their XRD patterns are given in Fig. 7a, where the remarkable changes of peaks emerge for the sodium titanate nanotubes after acidic treatment or the Ag^+ ion exchange processes. The peaks at around 9.89°, 28.39° and 61.13° appearing for the non-doped sodium titanate nanotubes nearly disappear after the acidic treatment whereas the peak near 24.28° increases. This is originated from the replacement of Na^+ ions by H^+ ions in the sample.[42] Specially, the Ag^+ ion exchange processes not only erase the peak at 9.89° but also destroy the peak at 24.28°. This might be attributed the staking disorder on the layered structure of titanate nanotubes caused by Ag^+ ion incorporation.[40a] The peak at 28.39° shifts to higher degrees, suggesting that Ag^+ ions are successfully intercalated into their interlayer position and bind more strongly with the TiO_6 layers than Na^+ ions.[41] Additionally, a shoulder upwarping reflection at 32–38° verifies the generation of Ag_2O (JCPDS no. 12-0793) nanoparticles, which corresponds to the results of SEM and TEM observations in Fig. 6. The Ag_2O is considered to be reduced to Ag during subsequent high temperature sintering processes in a N_2 atmosphere.

3.3. Nanobulks after sintering

The compositions and structures of samples after sintering were determined by XRD as shown in Fig. 7b. The sample deriving from the non-doped protonated titanate nanotubes (see curve a) is completely transformed into pure rutile-type TiO_2 (JCPDS no. 89-4920, space group: *P*42/*mnm*), while the Ag^+ ion exchanged specimens are the composites of TiO_2 and Ag. No other crystalline impurities are detected in the Nb-doped samples (see curve e). In addition, their peaks shift to lower degrees because of the slightly larger radius of Nb^{5+} ($r(Nb^{5+}) = 0.064$ nm) than that of Ti^{4+}, ($r(Ti^{4+}) = 0.0605$ nm),[43] indicating that the Nb-doping occurs by substitution of the Ti atoms. This result agrees with the case of heat treated samples in air as seen in Fig. 1d. However, the secondary phase $TiNb_2O_7$ is apparently not found for the samples sintered in a N_2 atmosphere, indicating that the solubility limit of Nb^{5+} into rutile in a N_2 atmosphere is higher than that in air.[44] Therefore, their reaction equations can be given as follows, where V^{4-} represents a vacancy with 4 negative charges and Nb^{5+} represents a Nb cation with positive 5 valances:

$$\frac{x}{2}Nb_2O_5 + (1-x)TiO_2 \xrightarrow{\text{Air}(600\,^\circ\text{C})} (V_{Ti}^{4-})_{\frac{x}{4}}Ti_{1-x}^{4+}Nb_x^{5+}O_2(\text{anatase}) + \frac{x}{4}O_2 \quad \text{(a)}$$

$$(0.03+z)Nb_2O_5 + (0.94+z)TiO_2 \xrightarrow{\text{Air}(900\,^\circ\text{C}),\ x>0.06} (V_{Ti}^{4-})_{0.015}Ti_{0.94}^{4+}Nb_{0.06}^{5+}O_2(\text{rutile}) + zTiNb_2O_7 + 0.015O_2 \quad \text{(b)}$$

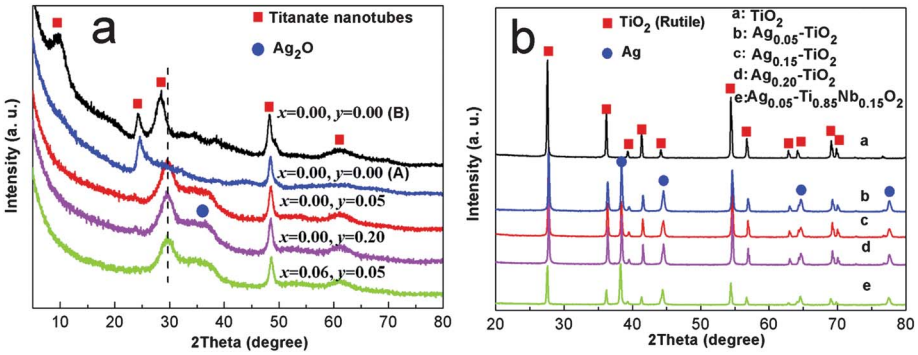

Fig. 7 XRD of the (a) alkaline, protonated and Ag^+ ions exchanged titanate nanostructures (in this figure, (B) represents sodium titanate nanotubes and (A) represents protonated titanate nanobutes) and (b) nanobulks after sintering.

$$\frac{x}{2}Nb_2O_5+(1-x)TiO_2 \xrightarrow{\text{Nitrogen}(1100\,^\circ\text{C})} Ti_x^{3+}Ti_{1-2x}^{4+}Nb_x^{5+}O_2(\text{rutile}) + \frac{x}{4}O_2 \quad (c)$$

Oxidative synthesis conditions in air might play in favor of the reactions described by the eqn (a) and (b), because both Ti and Nb cations maintain the highest oxidation states. The charge would be compensated by creating Ti cation vacancies. On the other hand, the reaction eqn (c) is considered for the reductive synthesis conditions in a N_2 atmosphere, where the Nb cations still keep the highest oxidation state. The charge equilibrium is realized by reducing Ti^{4+} to Ti^{3+}.[14,36a] The solubility limit of Nb^{5+} into rutile under the oxidative preparation conditions is about $x = 0.06$,[44,45] so the secondary phase $TiNb_2O_7$ is detected when the Nb concentration is high ($x > 0.06$, eqn (b)) just as exposed in Fig. 1f and e.

The morphologies of the samples are displayed in Fig. 8. The pure TiO_2 (see Fig. 8a) exhibits a flatter surface with boundary sizes of several microns than both the non-doped and Nb-doped composites as shown in Fig. 8b and c, respectively. Their corresponding high-magnified images in Fig. 8b_1 and c_1 show the clear features mentioned above. The Nb-doped cermet ($x = 0.06$) as given in Fig. 8c features more convex particles than the non-doped one in Fig. 8b. The EDX mapping of Ti, Nb and Ag and the line-scanning analysis along the part shown in Fig. 8c_2 are given in Fig. 8c_3–c_6, respectively. On all of the composites, Ag particles from about 50 nm to 2 μm are observed as exemplified in Fig. 8c_1.

It is worthwhile to point out that the oxygen vacancies (V^{2+} or Ti^{3+}) should be formed during the sintering process because of the high temperature and weak reductive atmosphere conditions. These vacancies might bring the oxygen-defect level in the band gap close to the conduction band of TiO_2, which could be responsible for the lower electrical resistivity of our obtained TiO_2 in contrast with stoichiometric TiO_2.[46]

3.4. Thermoelectric properties of the nanobulks

Fig. 9a gives the temperature-dependent electrical resistivities (ρ) for our samples. The ρ–T curves of non-doped samples are decreasing below 650 °C, suggesting a semiconducting behavior. However, they slightly rise as the temperature further increases. This may be attributed to the concentration of carrier being approximately invariable while the mobility decreases gradually. On the contrary, the ascending trend is not remarkable and the descending feature at low temperature becomes more and more distinct along with the increasing of Nb content for the Nb-doped specimens. In reality, all the samples roughly present activation-type transport in low temperature region where electrical conductivity is linearly dependent on $1000/T$ as shown in Fig. 9a_1. By using the relations[47] given by:

$$\rho = \rho_0 \exp(E_a/k_B T) \quad (1)$$

where k_B is the Boltzmann constant, the activation energy E_a can be calculated from this Arrhenius plot in Fig. 9a_1. The values depending on Nb and Ag content are listed in Table 3. They rise with increasing of Nb content and seem independent of Ag content (Table 3). These phenomena are ascribed to the fact that the Nb-doping level is stronger and farther away from the conduction band than the oxygen-defect level in the band gap. It is remarkable that the addition of both Ag and Nb reduce the electrical resistivity though different mechanisms take effect. The former perhaps mainly relies on the electrical connection between TiO_2 grains enhanced by Ag particles while the latter results from the increasing of carrier concentration contributed by the Nb^{5+} addition.

The Seebeck coefficients as a function of temperature are exhibited in Fig. 9b. All samples show negative values, indicating that they are n-type semiconductors. The enhancement of S is obvious after the introduction of Ag particles for the non-doped samples, in particular, the absolute value of $Ag_{0.05}$–TiO_2 increases by about 50 μV K^{-1} at temperatures higher than 500 °C. This can be explained by the theory of Faleev and Léonard,[17] where the thermopower is largely enhanced by the stronger scattering of low energy electrons than high energy electrons at the interface of semiconductor and metal. For the Nb-doped composites, at first, the effect caused by the change of Nb-doped TiO_2 granules' sizes is negligible because the variation of electronic scattering owing to the increasing of boundaries of Nb-doped grains is insignificant. Then, by using the following equation:[48]

$$|S| = -(k_B/e)\ln 10A(\log n_e + B) \quad (2)$$

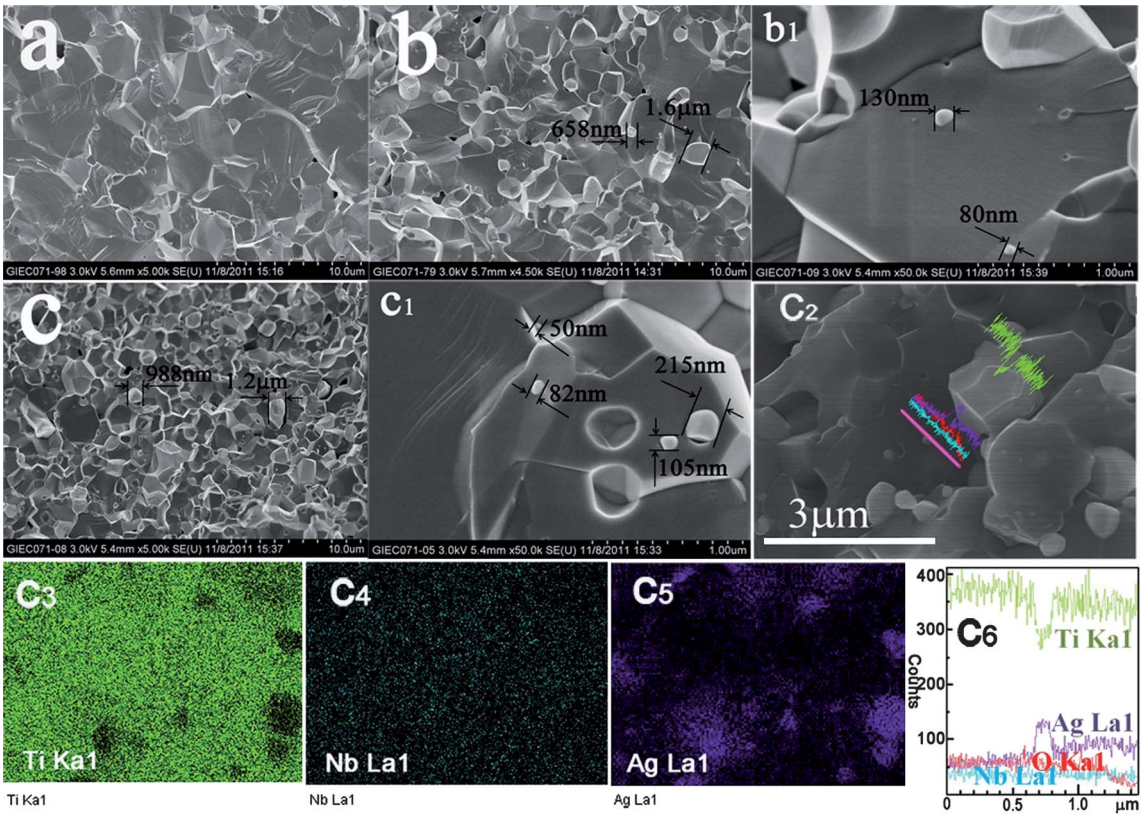

Fig. 8 SEM images of (a) TiO_2, (b) $Ag_{0.05}$–TiO_2 and (c) $Ag_{0.05}$–$Ti_{0.94}Nb_{0.06}O_2$ and high-magnified SEM micrographs of (b_1) $Ag_{0.05}$–TiO_2 and (c_1) $Ag_{0.05}$–$Ti_{0.94}Nb_{0.06}O_2$. An electron image (c_2) of $Ag_{0.05}$–$Ti_{0.94}Nb_{0.06}O_2$ selected to perform EDX analysis. Its corresponding elemental mapping of Ti (green), Nb (cyan) and Ag (purple) are shown in (c_3), (c_4) and (c_5), respectively, and line-scanning (indicated by the oblique line in (c_2)) result is displayed in (c_6). The particles whose sizes have been labeled in (b), (b_1), (c) and (c_1) are metallic Ag.

where A and B are intrinsic parameters determined by the types of materials and their energy band structures, it is convenient to identify the relationship between the absolute values of Seebeck coefficient ($|S|$) and carrier concentration (n_e). As shown in Fig. 9b_1, the slope of the $\log n_e - |S|$ plot for our samples is clearly steeper than that for the Nb-doped TiO_2 with anatase phase ($=-140$ μV K^{-1}).[49] Since the anatase and rutile phase have the same tetragonal TiO_6 system, it is reasonable to assume that they have nearly the same slope. Therefore, this deviation is presumably attributed to the effect of the Ag particles. Finally, it is easy to find that the content of Ag in the designated samples augments the activation energy when the Nb additive increases as shown in the third column of Table 3. This result suggests that large Ag particles may be abundant in the heavily Nb-doped specimens. This is responsible for the sharp decrease of thermopower with the increasing of electron concentration because large Ag grains are harmful to large Seebeck coefficients.

Accordingly, nanobulks display an apparent improved power factor in contrast with the case of pure TiO_2 as given in Fig. 9c. The maximum is obtained by $Ag_{0.05}$–$Ti_{0.94}Nb_{0.06}O_2$ and is about three times higher than that of the pure TiO_2. However, successively increasing Nb content results in the stagnation of power factors due to the non-compensatable decrease of S as described above.

Obviously, the introduction of Ag increases the thermal conductivity of composites as shown in Fig. 9d, which indicates the existence of large sized Ag particles. Generally speaking, Nb-doping hinders the growth of TiO_2 crystalline grains,[36a] which generates lots of boundaries to scatter middle and long wavelength phonons. That is why the thermal conductivity of Nb-doped samples is suppressed in low temperature region as shown in Fig. 9d. In spite of the partial counteraction by thermal conductivities, the values of ZT are still enhanced (see Fig. 9e). The maximal value of ZT is 0.082 at 973 K for the sample of $Ag_{0.05}$–$Ti_{0.94}Nb_{0.06}O_2$, which is about two times higher than that of TiO_2 (see Fig. 9e). This value is one of the better ones reported for n-type Ti-based thermoelectric materials.

3.5. Evolution mechanism of the nanobulks during sintering

The relationship between thermoelectric properties and the characteristics of metal particles (size and content) is intimate as described in Section 3.4. Therefore, it is worthwhile to summarize the evolution of semiconductor-metal composites during sintering processes for the prescription to the future efficient experiments. The schematic of it is illustrated in Fig. 10.

Unlike refractory TiO_2, whose melting point is about 1855 °C, noble metal Ag with a melting point of about 961 °C in the bulks is melted during our sintering procedures. The contact angle between the TiO_2 crystallites and the liquid Ag is greater than 90° in an inert atmosphere as described in the earlier literature,[50] so the Ag exists as liquid drops in the non-doped/Nb-doped TiO_2

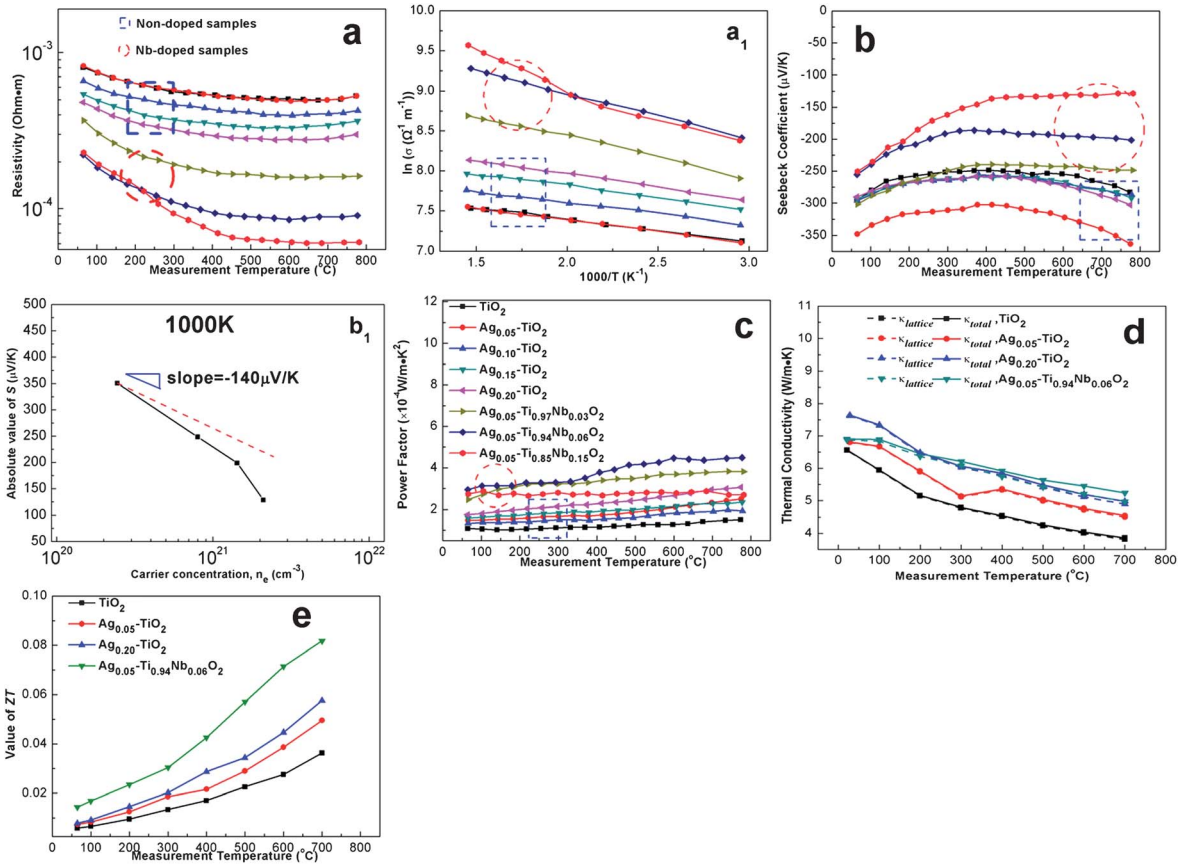

Fig. 9 Thermoelectric properties of the nanobulks: (a) electrical resistivity, (b) Seebeck coefficient, (c) power factor, (d) thermal conductivity (the lattice thermal conductivity is estimated by subtracting the corresponding electronic thermal conductivity whose value is calculated through the Wiedemann–Franz law: $\kappa_{electron} = L_0\sigma T$, where L_0 is the Lorentz constant equaling to 2.44×10^{-8} W Ω K^{-2}) and (e) value of ZT as a function of measurement temperature. (a_1) Arrhenius plot of electrical conductivity and (b_1) the relationship between carrier concentration (n_e) and absolute value of Seebeck coefficient (S) obtained from $Ag_{0.05}$–TiO_2, $Ag_{0.05}$–$Ti_{0.97}Nb_{0.03}O_2$, $Ag_{0.05}$–$Ti_{0.94}Nb_{0.06}O_2$ and $Ag_{0.05}$–$Ti_{0.85}Nb_{0.15}O_2$ (from left to right) at 1000 K, respectively. Here, the slope of Nb-doped TiO_2 with anatase phase from ref. 49 represented by the dotted line is given for comparison.

Table 3 Active energy (E_a) estimated by the Arrhenius plots shown in Fig. 3a$_1$ and atomic ratio of Ag to (Ti + Nb) calculated by using the analysis results of EDX spectra. The area selected for investigation of EDX spectra is 50 × 50 μm^2

Samples	Active energy (E_a)	Ratio of $n_{Ag}/(n_{Ti} + n_{Nb})$[a]
TiO_2	24 meV	0
$Ag_{0.05}$–TiO_2	25 meV	0.079
$Ag_{0.10}$–TiO_2	25 meV	0.098
$Ag_{0.15}$–TiO_2	25 meV	—
$Ag_{0.20}$–TiO_2	26 meV	0.129
$Ag_{0.05}$–$Ti_{0.97}Nb_{0.03}O_2$	45 meV	—
$Ag_{0.05}$–$Ti_{0.94}Nb_{0.06}O_2$	50 meV	0.112
$Ag_{0.05}$–$Ti_{0.85}Nb_{0.15}O_2$	81 meV	0.192

[a] The results of $Ag_{0.15}$–TiO_2 and $Ag_{0.05}$–$Ti_{0.97}Nb_{0.03}O_2$ are absent because they were not investigated.

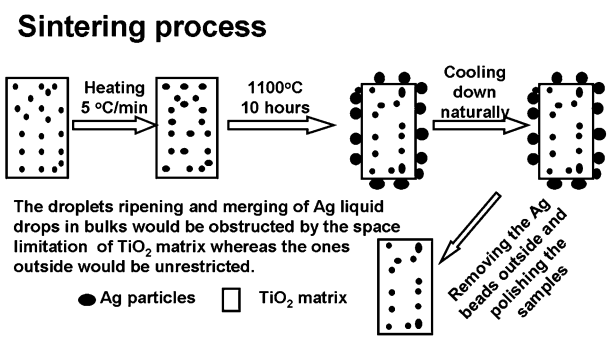

Fig. 10 Schematic illustration of the possible formation mechanism for nanobulks during the sintering processes. The droplets ripening and merging of Ag liquid drops embedded into the bulks would be obstructed by the space limitation of non-doped/Nb-doped TiO_2 matrix whereas the ones outside would be unrestricted.

matrix during the high temperature (1100 °C) sintering processes. In order to minimize the interfacial energy of the system, small liquid drops migrate to form bigger drops through two possible mechanisms: (1) mass exchange leading to collapse of the individual drops, and (2) the spatial movement resulting in the droplet collisions and the merging events.[51] However, the sizes of drops embedded into the matrix might be limited because of the space limitation imposed by the solid non-doped/Nb-doped TiO_2 matrix. Conversely, this limitation is absent on the surface of the matrix. Thus, melted Ag drops could be continuously extruded from inside the bulk composites.

Consequently, we can conclude that intensifying the space limitation of non-doped/Nb-doped TiO_2 matrix is effective to the formation of small-sized Ag particles, which improves thermoelectric properties (higher ZT). This could be realized by using higher pressure in cold-pressing procedures as well as accelerating the growth rate of TiO_2 during the heating processes.

4. Conclusion

In summary, an economical and environmentally-friendly hydrothermal reaction was proposed to prepare one-dimensional Nb-doped titanate nanostructures which also can be transformed into Nb-doped TiO_2 nanoparticles by a simple heat treatment in air. The formation mechanism of these nanostructures was discussed. During the hydrothermal reactions, very short sodium titanate nanotubes had been generated before Nb_2O_5 was activated. However, the co-precipitation of Nb^{5+} and Ti^{4+} ions definitely destroyed the formation of short nanotubes.

By using bottom-up assembly, Nb-doped TiO_2 nanobulks embedded with Ag nanoinclusions were successfully prepared by an aqueous ion exchange process and subsequent liquid phase sintering procedure in a N_2 atmosphere.

The introduction of Ag nanoparticles improved the thermoelectric performance of TiO_2-based ceramics, suggesting that these types of nanobulks can provide a pathway to search for promising thermoelectric materials. Furthermore, there remains large scope for the further enhancement of ZT by the optimization of the simple liquid phase sintering process or adopting other advanced sintering techniques. The evolution mechanism of our nanobulks proposed in this paper may also help to fabricate other metal–semiconductor nanobulks. In addition, our work indicates that combining nanostructuring and atomic doping is a good approach to enhance thermoelectric properties.

Acknowledgements

This work was supported by the National Natural Science Foundation of China (Grant No. 51172234), Guangdong Provincial Department of Science and Technology (Grant No. 2011B010100043), International Cooperation MOST-JST Program Fund (Grant No. 2010DFA61410) and No.y207k7.

References

1 (*a*) J. R. Sootsman, D. Y. Chung and M. G. Kanatzidis, *Angew. Chem., Int. Ed.*, 2009, **48**, 8616; (*b*) H. Kleinke, *Chem. Mater.*, 2010, **22**, 604.
2 P. Jood, R. J. Mehta, Y. Zhang, G. Peleckis, X. Wang, R. W. Siegel, T. Borca-Tasciuc, S. X. Dou and G. Ramanath, *Nano Lett.*, 2011, **11**, 4337.
3 S. Ohta, T. Nomura, H. Ohta, M. Hirano, H. Hosono and K. Koumoto, *Appl. Phys. Lett.*, 2005, **87**, 092108.
4 H. Kitagawa, T. Kunisada, Y. Yamada and S. Kubo, *J. Alloys Compd.*, 2010, **508**, 582.
5 I. Terasaki, Y. Sasago and K. Uchinokura, *Phys. Rev. B: Condens. Matter*, 1997, **56**, R12685.
6 (*a*) L. D. Hicks and M. S. Dresselhaus, *Phys. Rev. B: Condens. Matter*, 1993, **47**, 16631; (*b*) M. S. Dresselhaus, G. Chen, M. Y. Tang, R. Yang, H. Lee, D. Wang, Z. Ren, J. P. Fleurial and P. Gogna, *Adv. Mater.*, 2007, **19**, 1043.
7 L. Su and Y. X. Gan, *Electrochim. Acta*, 2011, **56**, 5794.
8 F. W. Dynys, M. -H. Berger and A. Sehirlioglu, *J. Am. Ceram. Soc.*, 2012, **95**, 619.
9 (*a*) B. Vijayan, N. M. Dimitrijevic, T. Rajh and K. Gray, *J. Phys. Chem. C*, 2010, **114**, 12994; (*b*) S. Chatterjee, K. Bhattacharyya, P. Ayyub and A. K. Tyagi, *J. Phys. Chem. C*, 2010, **114**, 9424.
10 (*a*) S. Yodyingyong, X. Y. Zhou, Q. F. Zhang, D. Triampo, J. T. Xi, K. Park, B. Limketkai and G. Z. Cao, *J. Phys. Chem. C*, 2010, **114**, 21851; (*b*) J. J. Qiu, F. W. Zhuge, K. Lou, X. M. Li, X. D. Gao, X. Y. Gan, W. D. Yu, H. K. Kim and Y. H. Hwang, *J. Mater. Chem.*, 2011, **21**, 5062.
11 (*a*) C. H. Han, D. W. Hong, I. J. Kim, J. Gwak, S. D. Han and K. C. Singh, *Sens. Actuators, B*, 2007, **128**, 320; (*b*) H. G. Liu, D. Y. Ding, C. Q. Ning and Z. H. Li, *Nanotechnology*, 2012, **23**, 015502.
12 (*a*) L. Kavan, M. Kalbác, M. Zukalová, I. Exnar, V. Lorenzen, R. Nesper and M. Graetzel, *Chem. Mater.*, 2004, **16**, 477; (*b*) A. R. Armstrong, G. Armstrong, J. Canales and P. G. Bruce, *Angew. Chem., Int. Ed.*, 2004, **43**, 2286.
13 Y. D. Wang, B. M. Smarsly and I. Djerdj, *Chem. Mater.*, 2010, **22**, 6624.
14 X. J. Lü, X. L. Mou, J. J. Wu, D. W. Zhang, L. L. Zhang, F. Q. Huang, F. F. Xu and S. M. Huang, *Adv. Funct. Mater.*, 2010, **20**, 509.
15 Y. J. Liu, J. M. Szeifert, J. M. Feckl, B. Mandlmeier, J. Rathousky, O. Hayden, D. Fattakhova-Rohlfing and T. Bein, *ACS Nano*, 2010, **4**, 5373.
16 N. R. Elezovic, B. M. Babic, V. R. Radmilovic, L. M. Vracar and N. V. Krstajic, *Electrochim. Acta*, 2011, **56**, 9020.
17 S. V. Faleev and F. Léonard, *Phys. Rev. B: Condens. Matter Mater. Phys.*, 2008, **77**, 214304.
18 N. V. Nong, N. Pryds, S. Linderoth and M. Ohtaki, *Adv. Mater.*, 2011, **23**, 2484.
19 M.-K. Han, K. Ahn, H. J. Kim, J.-S. Rhyee and S.-J. Kim, *J. Mater. Chem.*, 2011, **21**, 11365.
20 J. S. Moya, S. Lopez-Esteban and C. Pecharroman, *Prog. Mater. Sci.*, 2007, **52**, 1017.
21 R. J. Mehta, Y. J. Zhang, C. Karthik, B. Singh, R. W. Siegel, T. Borca-Tasciuc and G. Ramanath, *Nat. Mater.*, 2012, **11**, 233.
22 L. Miao, S. Tanemura, R. Huang, C. Y. Liu, C. M. Huang and G. Xu, *ACS Appl. Mater. Interfaces*, 2010, **2**, 2355.
23 K. Yoshida, L. Miao, N. Tanaka and S. Tanemura, *Nanotechnology*, 2009, **20**, 405709.
24 D. V. Bavykin, A. N. Kulak and F. C. Walsh, *Cryst. Growth Des.*, 2010, **10**, 4421.
25 J. Q. Huang, Y. G. Cao, M. L. Wang, C. G. Huang, Z. H. Deng, H. Tong and Z. G. Liu, *J. Phys. Chem. C*, 2010, **114**, 14748.
26 (*a*) W. B. Hu, L. P. Li, G. S. Li, J. Meng and W. M. Tong, *J. Phys. Chem. C*, 2009, **113**, 16996; (*b*) G. S. Li, L. P. Li, J. Boerio-Goates and B. F. Woodfield, *J. Am. Chem. Soc.*, 2005, **127**, 8659.
27 X. M. Sun and Y. D. Li, *Chem.–Eur. J.*, 2003, **9**, 2229.
28 V. Shanker, S. L. Samal, G. K. Pradhan, C. Narayana and A. K. Ganguli, *Solid State Sci.*, 2009, **11**, 562.
29 (*a*) H. C. Zeng and S. K. Tung, *Chem. Mater.*, 1996, **8**, 2667; (*b*) J. F. Liu, X. L. Li and Y. D. Li, *J. Cryst. Growth*, 2003, **247**, 419; (*c*) G. Bhagavannarayana, G. C. Budakoti, K. K. Maurya and B. J. Kumar, *J. Cryst. Growth*, 2005, **282**, 394.
30 (*a*) M. Qamar, C. R. Yoon, H. J. Oh, D. H. Kim, J. H. Jho, K. S. Lee, W. J. Lee, H. G. Lee and S. J. Kim, *Nanotechnology*, 2006, **17**, 5922; (*b*) T. Gao, H. Fjellvag and P. Norby, *Inorg. Chem.*, 2009, **48**, 1423; (*c*) S. J. Kim, Y. U. Yun, H. J. Oh, S. H. Hong, C. A. Roberts, K. Routray and I. E. Wachs, *J. Phys. Chem. Lett.*, 2010, **1**, 130.
31 E. R. Camargo, M. Popa and M. Kakihana, *Chem. Mater.*, 2002, **14**, 2365.
32 H. Y. Zhu, Z. F. Zhang, X. P. Gao, Y. P. Huang, Z. M. Yan, J. Zou, H. M. Yin, Q. D. Zou, S. H. Kable, J. C. Zhao, Y. F. Xi, W. N. Martens and R. L. Frost, *J. Am. Chem. Soc.*, 2006, **128**, 2373.
33 D. Wu, J. Liu, X. Zhao, A. Li, Y. Chen and N. Ming, *Chem. Mater.*, 2006, **18**, 547.
34 S. Y. Wu, W. Zhang and X. M. Chen, *J. Mater. Sci.: Mater. Electron.*, 2010, **21**, 450.
35 (*a*) R. Ma, K. Fukuda, T. Sasaki, M. Osada and Y. Bando, *J. Phys. Chem. B*, 2005, **109**, 6210; (*b*) C. C. Tsai and H. Teng, *Chem. Mater.*, 2006, **18**, 367.
36 (*a*) A. M. Ruiz, J. Dezanneau, J. Arbiol, A. Cornet and J. R. Morante, *Chem. Mater.*, 2004, **16**, 862; (*b*) S. Phanichphant, C. Liewhiran, K. Wetchakun, A. Wisitsoraat and A. Tuantranont, *Sensors*, 2011, **11**, 472.
37 (*a*) B. D. Yao, Y. F. Chan, X. Y. Zhang, W. F. Zhang, Z. Y. Yang and N. Wang, *Appl. Phys. Lett.*, 2003, **82**, 281; (*b*) Y. Q. Wang, G. Q. Hu, X. F. Duan, H. L. Sun and Q. K. Xue, *Chem. Phys. Lett.*, 2002, **365**, 427.

38 Y. Lan, X. P. Gao, H. Y. Zhu, Z. F. Zheng, T. Y. Yan, F. Wu, S. P. Ringer and D. Y. Song, *Adv. Funct. Mater.*, 2005, **15**, 1310.
39 D. V. Bavykin, V. N. Parmon, A. A. Lapkin and F. C. Walsh, *J. Mater. Chem.*, 2004, **14**, 3370.
40 (*a*) J. A. Toledo-Antonio, M. A. Cortes-Jácome, C. Angeles-Chavez, E. López-Salinas and P. Quintana, *Langmuir*, 2009, **25**, 10195; (*b*) H. B. Li, X. C. Duan, G. C. Liu and X. Q. Liu, *J. Mater. Sci.*, 2008, **43**, 1669; (*c*) I. Bracko, B. Jancar, M. Logar, D. Caglic and D. Suvorov, *Nanotechnology*, 2011, **22**, 085705.
41 (*a*) R. Z. Ma, T. Sasaki and Y. Bando, *J. Am. Chem. Soc.*, 2004, **126**, 10382; (*b*) F. Cesano, S. Bertarione, M. J. Uddin, G. Agostini, D. Scarano and A. Zecchina, *J. Phys. Chem. C*, 2010, **114**, 169.
42 (*a*) C. C. Tsai and H. Teng, *Chem. Mater.*, 2006, **18**, 367; (*b*) J. Yang, Z. Jin, X. Wang, W. Li, J. Zhang, S. Zhang, X. Guo and Z. Zhang, *Dalton Trans.*, 2003, 3898.
43 R. D. Shannon, *Acta Crystallogr., Sect. A: Cryst. Phys., Diffr., Theor. Gen. Crystallogr.*, 1976, **32**, 751.
44 M. Valigi, D. Cordischi, G. Minelli, P. Natale, P. Porta and C. P. Keijzers, *J. Solid State Chem.*, 1988, **77**, 255.
45 K. Zakrzewska, M. Radecka and M. Rekas, *Thin Solid Films*, 1997, **310**, 161.
46 T. Bak, M. K. Nowotny, L. R. Sheppard and J. Nowotny, *J. Phys. Chem. C*, 2008, **112**, 7255.
47 Y. Nagao, I. Terasaki and T. Nakano, *Phys. Rev. B: Condens. Matter Mater. Phys.*, 2007, **76**, 144203.
48 H. Ohta, K. Sugiura and K. Koumoto, *Inorg. Chem.*, 2008, **47**, 8429.
49 D. Kurita, S. Ohta, K. Sugiura, H. Ohta and K. Koumoto, *J. Appl. Phys.*, 2006, **100**, 096105.
50 J. G. Li and J. C. Gao, *Mater. Lett.*, 2006, **60**, 1323.
51 K. B. Glasner and T. P. Witelski, *Phys. D*, 2005, **209**, 80.

